Surface Science

DOI: 10.1002/ange.201108532

Direct Observation of Surface Reconstruction and Termination on a Complex Metal Oxide Catalyst by Electron Microscopy**

*Yihan Zhu, Qingxiao Wang, Lan Zhao, and Yu Han**

Selective conversion of light hydrocarbons using complex metal oxide (CMO) catalysts has attracted great research attention in the past decades.[1] Bulk crystalline structures of CMOs are investigated and correlated with their catalytic performance in most studies,[2] whereas it is increasingly realized that anomalous surface termination modes, such as reconstruction,[3] metal–oxygen bond relaxation,[4] clustering,[5] defects[6] and amorphous components,[7] play crucial roles in catalytic activity. Despite some sound surface models having been proposed for simple oxides,[8] the forms of surface termination in CMO catalysts and their physical origins remain controversial, owing to the difficulty of directly observing the atomic structures of the outmost surface.

Among various CMOs, MoVTe(Nb)O catalysts have received special attention for their ability to convert abundant and low-cost propane into high value-added oxygenates (e.g. acrolein (ACR),[9] acrylic acid (AA),[10] and acrylonitrile (ACN)[10a]) by selective (amm)oxidation, which allows upgrading the conventional propylene-based BP/SOHIO process.[11] Two major active phases of the MoVTe(Nb)O catalyst, orthorhombic M1 phase (*Pba*2) and pseudo-hexagonal (orthorhombic) M2 phase (*P*6*mm* or *Pmm*2), have been extensively studied with an emphasis on the correlation between their crystal structures and catalytic activities.[2a,c] Both M1 and M2 phases possess layered structure and regular arrays of one-dimensional (1D) channels along the [001] direction that are partially occupied by $\{TeO_x\}$ (and $\{NbO_x\}$) entities.[12] The major difference between them is within the (001) crystal plane, in which corner-sharing MO_6 ($M = Mo$ or V) octahedra enclose hepta-, hexa-, and pentagonal channels in the M1 phase but solely hexagonal ones in the M2 phase (Figure S1 in the Supporting Information). Atomic-scale studies of the anisotropic surface chemistry of these active phases would help to understand their outstanding catalytic performance.

With modern electron microscopy (EM) techniques, direct observation of individual atomic columns becomes possible.[13] In a recent study by Su's group,[14] the outmost surface structure of the M1 phase was imaged by high-angle-annular-dark-field scanning transmission electron microscopy (HAADF-STEM), showing little difference from the bulk crystal structure[12] and only a small extent of structural relaxation that generates terminal M=O from fractured M−O bonds. This result is in line with the high catalytic activity of M1 phase.[14] However, the surface chemistry of the M2 phase is yet unknown and is believed to account for its puzzling catalytic behavior, for example: 1) pure M2 phase is active towards α-C−H bonds but inactive towards saturated C−H bonds;[15] 2) M2 phase has a "synergetic effect" with the M1 phase when used for propane (amm)oxidation, enhancing the selectivity towards AA/ACN;[15,16] 3) M2 phase replenishes the tellurium loss of the M1 phase during the reactions, effectively avoiding its quick deactivation.[16a] In this study, we make use of advanced electron microscopic sample preparation and imaging techniques to observe directly the surface termination of the M2 phase, and hereby propose a surface reconstruction model to explain its catalytic behavior.

A Nb-free MoVTeO M2 phase was synthesized by the slurry method. It consists of hexagonal prism-shaped crystals with the (001) basal and {hk0} prismatic facets exposed (Figure S2 in the Supporting Information). A surface termination study by EM requires an ultrathin specimen with identifiable surface of the catalyst. To this end, we applied the focused ion beam (FIB) technique, which allows site-specific sample preparation by selectively cutting the desired region out of the catalyst crystal to ensure that the obtained specimen contains the "real" outmost surface. This method was used to prepare a thin specimen that represents a cross-section of the M2 hexagonal prism crystal along the [001] axis and contains both the basal and prismatic surfaces (Figure S3 in the Supporting Information and Figure 1 a).

Surface termination on the (001) basal plane was examined with transmission electron microscopy (TEM), which revealed a thin nanocrystalline layer extending out of the bulk crystal by ca. 15 nm (Figure 1 a, inset). A high-resolution TEM image recorded near the Scherzer defocus showed narrow lattice fringes ($d = 3.15$ Å) in the nanocrystalline layer terminating the (110) lattice fringes of M2 phase bulk crystal ($d = 6.31$ Å) with good lattice matching, where the projection of M2 phase was determined to be the $[1\bar{1}\bar{2}]$ direction (Figure 1 c). The grain boundary between two phases is indicated by red arrows in Figure 1 b. These results suggest that surface reconstruction occurs on the (001) surface of M2 phase, but it is difficult to identify the reconstructed phase by TEM because the nanocrystalline layer is very beam sensitive, inhibiting the image acquirement for difference zone axes by tilting series. However, we noticed some interesting phenom-

---

[*] Y. Zhu, Prof. Y. Han
Advanced Membranes and Porous Materials Center, Chemical and Life Science and Engineering Division, King Abdullah University of Science and Technology, Thuwal 23955-6900 (Saudi Arabia)
E-mail: yu.han@kaust.edu.sa

Q. Wang, L. Zhao
Core Lab of Imaging and Characterization
King Abdullah University of Science and Technology
Thuwal 23955-6900 (Saudi Arabia)

[**] This research was supported by the baseline research fund from King Abdullah University of Science and Technology.

Supporting information for this article is available on the WWW under http://dx.doi.org/10.1002/anie.201108532.

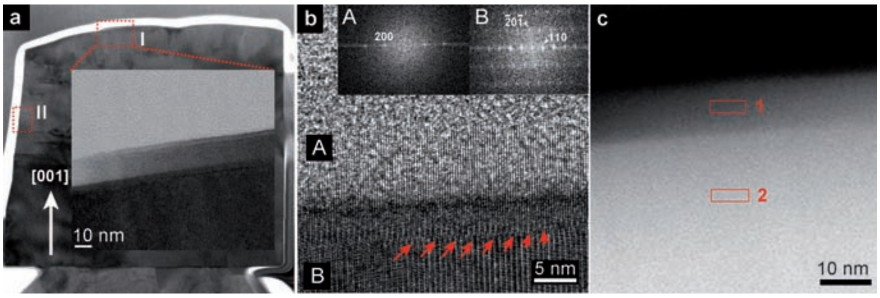

Figure 1. a) Low-magnification STEM image of the prepared specimen in which regions I and II were used to investigate the basal and prismatic surface termination, respectively. The inset shows a TEM image of region I. b) HRTEM image of region I, showing a nanocrystalline layer (A) with thin lattice fringes that terminates the (001) surface of the M2 phase (B). The insets show the corresponding fast Fourier transforms (FFT); Red arrows indicate the grain boundary between the two phases. c) STEM image of the same specimen, where two areas are respectively selected from the nanocrystalline layer and bulk M2 phase for EDX spectroscopic analysis (see Figure S6 in the Supporting Information for spectra).

ena: 1) a trace amount of $VOMoO_4$ (tetragonal P4/*n*, $a=6.607$ and $c=4.264$ Å) always accompanies the MoVTeO M2 phase synthesized under different conditions, and its content increases with the calcination time and temperature (Figure S4); 2) the crystal lattices of M2 and $VOMoO_4$ match well in certain orientations with very close interplanar distances, for example, $d_{\{110\}}$, $d_{\{201\}}$, and $d_{\{221\}}$ in M2 phase coincide with $2d_{\{200\}}$, $d_{\{111\}}$, and $d_{\{221\}}$ in $VOMoO_4$, respectively; 3) the Te species is gradually lost from the surface of MoVTe(Nb)O type catalysts upon heating.[16a,17] On the basis of these observations, we speculate that the observed nanocrystalline layer is $VOMoO_4$ generated from M2 phase by reconstruction of the outmost (001) surface accompanied with Te loss, and such a phase transition is facilitated by heating. It should be noted that the nanocrystalline layer cannot be identified as a new phase just from a single TEM image because the image contrast varies with specimen thickness that may result in an illusion, and very thin M2 phase could give similar contrast. The lattice fringes of 3.15 Å can be assigned to either d_{220} of M2 phase or d_{200} of $VOMoO_4$. However, the former is ruled out by the absence of (110) reflections in the fast Fourier transform (FFT) results (Figure 1 b and Figure S5), while the latter assignment is reasonable given that the (100) reflections of $VOMoO_4$ are extinct. Energy-dispersive X-ray spectroscopy (EDX) was combined with STEM for micro-region elemental analysis of the same specimen (Figure 1 c). The results show that the nanocrystalline region has a lower Mo/V atomic ratio than the bulk M2 phase (Figure S6), which is consistent with the hypothesis that it is composed of $VOMoO_4$.

To further verify this hypothesis, we used environmental SEM (ESEM) equipped with a thermal stage to observe in situ surface morphology changes of the as-synthesized M2 phase upon heating. The surface morphology of M2 crystal did not exhibit a visible change at 673 K, while further increasing the temperature to 873 K resulted in the generation of discrete islands over the entire (001) crystal surface (Figure 2). With prolonged heating, nanoislands grew further into large crystals. Compared to the thin nanocrystalline layer observed in as-synthesized M2 phase, the bulk crystals (islands) formed by post-heating M2 phase are more suitable for structural identification by EM for their higher stability. Hence, we again used the FIB technique to prepare a specimen from a post-calcined (at 873 K) sample that involved both the original substrate crystal and the newly grown islands (Figure 3 a), and then characterized the two regions with HAADF-STEM (Figure 3 b,c). By indexing the FFT results

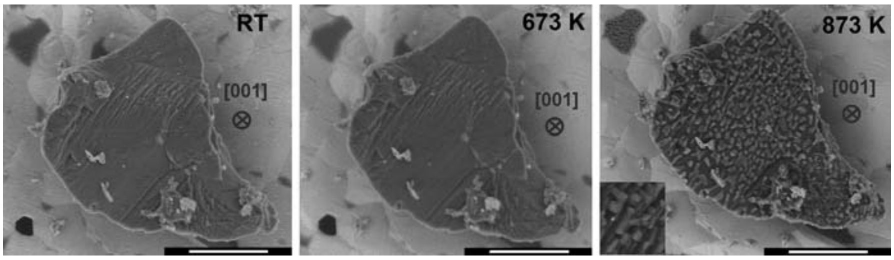

Figure 2. In situ environmental SEM images of a M2 phase crystal at various temperatures, showing the basal surface morphology change upon heating. The inset shows an enlarged image of the nanoislands generated at 873 K. The scale bars correspond to 5 μm.

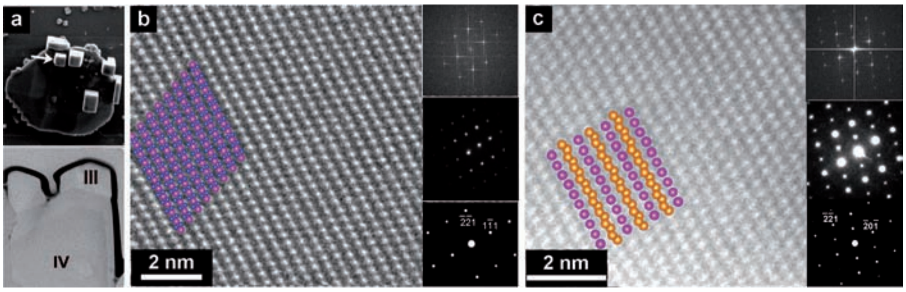

Figure 3. a) SEM image of a M2 phase crystal after post-calcination at 873 K for 2 h (top), from which a EM specimen is fabricated by FIB containing both the bulk crystal and newly generated nanoislands (bottom). The arrow indicates the location of specimen preparation. b) HR-STEM image of the nanoisland taken along the $[1\bar{3}\bar{4}]$ direction and superimposed by the structural model of $VOMoO_4$ (purple: MoO; blue: VO). c) HR-STEM image of the bulk crystal taken along the $[1\bar{2}\bar{2}]$ direction and superimposed by the structural model of the M2 phase (purple: MO; orange: TeMO). The insets (from the top down) are the corresponding FFTs, as well as experimental and simulated electron diffraction patterns, respectively.

and selected-area electron diffraction (SAED) patterns, it was determined that the substrate crystal and the island belong to M2 phase (along the $[1\bar{2}\bar{2}]$ projection) and $VOMoO_4$ phase (along the $[1\bar{3}\bar{4}]$ projection), respectively. Furthermore, comparison of the linear intensity profiles extracted from the STEM images and the simulated ones confirms the phase identification made above (Figure S7). As determined from Figure 3, the $[1\bar{1}1]^*$ axis of $VOMoO_4$ coincides with the $[\bar{2}0\bar{1}]^*$ axis of M2 phase. It is thus deduced that the projection of the nanocrystalline $VOMoO_4$ in Figure 1 c is along the $[0\bar{1}\bar{1}]$ axis (Figure S8). A possible reason for the appearance of only one set of lattice fringes ($d_{\{200\}} = 3.15$ Å, Figure 1 c) in this projection is the bending of thin nanocrystalline layer.

The synthetic precursor of the M2 phase was heated to various temperatures, and the evolution of surface oxido–tellurium species was traced by in situ Raman spectroscopy. It is observed that new bands at 708.2 cm^{-1} and 721.3 cm^{-1} occur at 673 K that can be assigned to the A_1 and B_1 vibration modes of C_{2v} symmetric TeO_4E species (Figure 4 a and Table S1). In the M2 phase, C_s symmetric TeO_3E coexists with TeO_4E in dynamic equilibrium,[12,18] but its Raman band (A′ mode) is indistinguishable from the B_1 band of TeO_4E in the spectra. Meanwhile, metallic Te is produced, as evidenced by the 120.7 cm^{-1} (A_1 mode) and 140.0 cm^{-1} (E_{TO} mode) bands.[19] Further elevating the temperature gradually broadens the A_1 and B_1 (A′) bands of oxido–tellurium species, causing them to merge. At 873 K, that is the synthesis temperature of the M2 phase, in most studies, the degeneration of A_1 and B_1 (A′) bands to the 717.1 cm^{-1} band (T_2 mode) was observed, indicating a major transition of interacted (with the MO_6 framework) oxido–tellurium species (i.e. TeO_4E and TeO_3E) to isolated T_d symmetric TeO_4 species on the surface (Table S1). Moreover, sublimation products are observed at 873 K, which were determined to comprise metallic Te and $MoTe_2$ (Figure S9).[19,20] These results imply that oxido–tellurium species start to form an ordered structure at 673 K and simultaneously undergo a surface redox reaction that is further promoted with elevated temperature. It is well known that oxygen hopping can take place along a 1D chain of cations with alternating stereoactive ns^2 electron lone pairs and oxygen anions.[21] We propose that in the M2 phase, such oxygen hopping along the 1D chain of tellurium oxido species in the M_6O_6 (M = Mo or V) channels promoted by high-temperature calcinations would terminate on the outmost (001) surface to produce pairs of isolated Te^{6+} and Te^{2+} oxido species. The unstable Te^{2+} species would extract two electrons from the framework to form Te^0 metallic species (Figure 4 b). The loss of Te from the outmost surface induces its reconstruction to $VOMoO_4$. X-ray photoemission spectroscopy (XPS) conducted on the as-synthesized M2 phase indicated the presence of V^{4+}, Mo^{6+}, and Te^{6+} species on the outmost surface (Figure S10), supporting the above proposed mechanism.

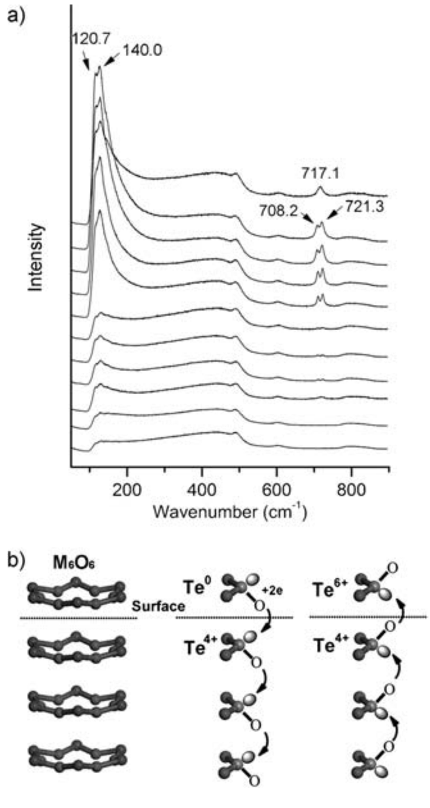

Figure 4. a) In situ Raman spectra of the M2 phase synthetic precursor heated in nitrogen flow to various temperatures (from the bottom up: room temperature, 373, 473, 523, 573, 623, 673, 723, 773, 823, and 873 K). b) Schematic illustration of the proposed surface termination mechanism. The left column represents the M_6O_6 channels, while the right two columns depict oxygen hopping in the channels that induces the disproportionation of oxido–tellurium species at the outmost (001) surfaces and thus the reconstruction.

The termination of the prismatic surface was also studied with HAADF-STEM. In the image taken along the $[1\bar{1}0]$ direction, the lattice in parallel to [001] direction showed alternating strong–weak contrast, corresponding to TeMO and MO atomic columns, respectively (Figure 5). The outmost amorphous region along the [110]* direction is the deposited Pt/C protection layer for FIB sample preparation. As clearly illustrated in Figure 5, the M2 structure uniformly spreads along the [110]* direction to the outmost surfaces

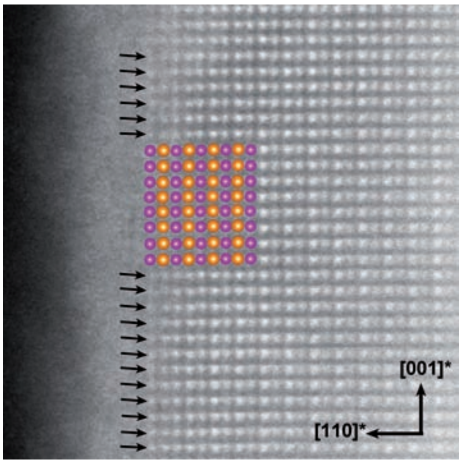

Figure 5. HR-STEM image of region II in Figure 1 a taken along the $[1\bar{1}0]$ direction and superimposed with the M2 phase structural model (purple: MO; orange: TeMO).

without reconstructing into other crystalline structures. In addition, the STEM images show that the prismatic surface is mainly terminated by the MO columns, as indicated by the arrows in Figure 5, suggesting the inaccessibility of multifunctional sites on the prismatic surfaces.

The (001) surface reconstruction of M2 phase to $VOMoO_4$ results in the outmost surfaces comprising $V^{4+}O_6$ octahedral and $Mo^{6+}O_4$ tetrahedral sites. The absence of $V^{5+}{=}O$ on the (001) surfaces explains the low catalytic activity of M2 phase against propane as the strongly polarized $V^{5+}{=}O$ species are critical for initial activation of saturated C–H bonds.[2a,c] It is widely accepted that Te^{4+} and Te^{6+} oxido species are the active sites for α-C–H bond activation,[2a,c] and responsible for the selective oxidation of propylene.[15] In comparison with the bulk Te^{4+} oxido species strongly interacted with the framework,[22] the large amount of isolated $Te^{6+}O_4$ oxido species observed on the surface of the M2 phase have a higher valence state with more active oxygen, and are therefore more efficient in converting dehydrogenated intermediates (e.g. propylene) to target oxygenates. Thus, the surface $Te^{6+}O_4$ oxido species would facilitate the selective oxidation reaction pathway and account for the high selectivity towards acrylic acid or acrylonitrile that the M2 phase exhibits for propylene oxidation.[15] When the M2 phase is used along with the M1 phase as a co-catalyst for propane (amm)oxidation, the highly mobile isolated $Te^{6+}O_4$ species may migrate from M2 surface to M1 surface through the intimate grain-to-grain contact, which not only replenishes the oxido–tellurium sites lost during the reaction but also increases the selectivity of acrylic acid or acrylonitrile. This explains the observed "synergetic effect".

It is worth noting that although surface reconstruction may start with the M2 phase structure formation from 673 K, it becomes remarkable only at higher temperature. Hence, the active $Te^{6+}O_4$ surface species are mainly formed at 873 K employed for the M2 phase synthesis (Figure 4a), and would be gradually depleted during the catalytic reactions, which are usually carried out at a lower temperature of 673 K. As a result, the "synergetic effect" only appears in a limited reaction time and propane conversion window.[16b] This conclusion was confirmed by characterizing the used M2 phase catalyst (at 673 K for 6 h) with Raman and XRD analysis. The disappearance of T_2 band in the Raman spectrum in comparison with the as-synthesized catalyst suggests the depletion of surface-active $Te^{6+}O_4$ species (Figure S11), while little change in the XRD pattern indicates negligible phase transition during the reaction (Figure S12).

In summary, FIB was employed to prepare a specimen from a complex metal oxide catalyst (M2 phase), which allows us to investigate its surface termination by electron microscopy. Various characterization methods were combined to demonstrate the presence of nanocrystalline $VOMoO_4$ in the as-synthesized M2 phase that terminates the (001) surface and would further evolve into bulk crystals by prolonged heating at 873 K. We propose that during the synthesis of the M2 phase, $VOMoO_4$ is inevitably produced by the surface reconstruction of the M2 phase, as a result of a surface redox reaction, that is, the disproportionation of oxido–tellurium species. The proposed surface reconstruction model explains well the puzzling catalytic behavior of the M2 phase observed in practical applications.

Experimental Section

The MoVTeO complex metal oxide M2 phase was synthesized by the slurry method. The (S)TEM specimen was fabricated on an FEI Helios NanoLab 400S FIB/SEM dual-beam system using Pt/C deposition for sample protection. Environmental in situ SEM was conducted on an FEI Quanta 600 microscope with a gaseous secondary electron detector operated at 5 KV. HRTEM images were acquired on an FEI Titan ST electron microscope ($C_s = 1.2$ mm; $C_c = 1.5$ mm; 300 kV). HAADF-STEM images were taken on a cubed Titan G2 electron microscope with probe-corrector operated at 300 kV. The inner and outer electron collecting angle of the HAADF detector was set to be 80 and 400 mrad respectively, and the probe semi-convergence angle was 24.9 mrad. The S/TEM simulation was carried out with CrystalKit™ and MacTempas™ bundle programs based on the multislice method. Detailed synthesis and characterization methods are provided in the Supporting Information.

Received: December 2, 2011
Revised: January 23, 2012

Keywords: electron microscopy · heterogeneous catalysis · solid-state structures · surface chemistry · transition metals

---

[1] a) R. K. Grasselli, A. A. Tenhover, in *Handbook of Heterogeneous Catalysis*, *Vol. 7*, 2nd ed. (Eds.: G. Ertl, H. Knözinger, F. Schüth, J. Weitkamp), Wiley-VCH, Weinheim, **2008**, p. 3489; b) R. K. Grasselli, J. D. Burrington in *Handbook of Heterogeneous Catalysis*, *Vol. 7*, 2nd ed. (Eds.: G. Ertl, H. Knözinger, F. Schüth, J. Weitkamp), Wiley-VCH, Weinheim, **2008**, p. 3479.

[2] a) R. K. Grasselli, D. J. Buttrey, P. DeSanto, J. D. Burrington, C. G. Lugmair, A. F. Volpe, T. Weingand, *Catal. Today* **2004**, *91–92*, 251–258; b) J. Ziokowski, E. Bordes, P. Courtine, *J. Catal.* **1990**, *122*, 126–150; c) R. K. Grasselli, J. D. Burrington, D. J. Buttrey, P. DeSanto, C. G. Lugmair, A. F. Volpe, T. Weingand, *Top. Catal.* **2003**, *23*, 5–22.

[3] a) C. Barth, M. Reichling, *Nature* **2001**, *414*, 54–57; b) J. B. Wagner, S. B. Abd Hamid, D. Othman, O. Timpe, S. Knobl, D. Niemeyer, D. S. Su, R. Schlogl, *J. Catal.* **2004**, *225*, 78–85.

[4] F. Gilardoni, A. T. Bell, A. Chakraborty, P. Boulet, *J. Phys. Chem. B* **2000**, *104*, 12250–12255.

[5] a) G. Deo, I. E. Wachs, J. Haber, *Crit. Rev. Surf. Chem.* **1994**, *4*, 141–187; b) I. E. Wachs, B. M. Weckhuysen, *Appl. Catal. A* **1997**, *157*, 67–90.

[6] P. L. Gai, K. Kourtakis, *Science* **1995**, *267*, 661–663.

[7] a) G. J. Hutchings, J. A. Lopez-Sanchez, J. K. Bartley, J. M. Webster, A. Burrows, C. J. Kiely, A. F. Carley, C. Rhodes, M. Havecker, A. Knop-Gericke, R. W. Mayer, R. Schlogl, J. C. Volta, M. Poliakoff, *J. Catal.* **2002**, *208*, 197–210; b) K. Routray, W. Zhou, C. J. Kiely, I. E. Wachs, *ACS Catal.* **2011**, *1*, 54–66.

[8] a) M. M. Lin, *Appl. Catal. A* **2003**, *250*, 305–318; b) J. Haber, E. Lalik, *Catal. Today* **1997**, *33*, 119–137.

[9] Y. H. Zhu, W. M. Lu, H. Li, H. L. Wan, *J. Catal.* **2007**, *246*, 382–389.

[10] a) H. Tsuji, Y. Koyasu, *J. Am. Chem. Soc.* **2002**, *124*, 5608–5609; b) T. Ushikubo, H. Nakamura, Y. Koyasu, S. Wajiki, U.S. Patent 5380 933, **1995**.

[11] R. K. Grasselli, A. A. Tenhover in *Handbook of Heterogeneous Catalysis*, *Vol. 7*, 2nd ed. (Eds.: G. Ertl, H. Knözinger, F. Schüth, J. Weitkamp), Wiley-VCH, Weinheim, **2008**, p. 2303.

[12] P. DeSanto, D. J. Buttrey, R. K. Grasselli, C. G. Lugmair, A. F. Volpe, B. H. Toby, T. Vogt, *Z. Kristallogr.* **2004**, *219*, 152–165.

[13] S. Y. Choi, S. Y. Chung, T. Yamamoto, Y. Ikuhara, *Adv. Mater.* **2009**, *21*, 885.

[14] W. Zhang, A. Trunschke, R. Schlogl, D. S. Su, *Angew. Chem.* **2010**, *122*, 6220–6225; *Angew. Chem. Int. Ed.* **2010**, *49*, 6084–6089.

[15] J. Holmberg, R. K. Grasselli, A. Andersson, *Appl. Catal. A* **2004**, *270*, 121–134.

[16] a) M. Baca, M. Aouine, J. L. Dubois, J. M. M. Millet, *J. Catal.* **2005**, *233*, 234–241; b) P. Korovchenko, N. R. Shiju, A. K. Dozier, U. M. Graham, M. O. Guerrero-Perez, V. V. Guliants, *Top. Catal.* **2008**, *50*, 43–51.

[17] J. M. Oliver, J. M. L. Nieto, P. Botella, A. Mifsud, *Appl. Catal. A* **2004**, *257*, 67–76.

[18] Y. Himei, A. Osaka, T. Nanba, Y. Miura, *J. Non-Cryst. Solids* **1994**, *177*, 164–169.

[19] A. S. Pine, G. Dresselhaus, *Phys. Rev. B* **1971**, *4*, 356.

[20] Raman Spectra Database of Minerals and Inorganic Materials, National Institute of Advanced Industrial Science and Technology (AIST).

[21] J. Galy, R. Enjalbeft, P. Rozier, P. Millet, *Solid State Sci.* **2003**, *5*, 165–174.

[22] M. Baca, J. M. M. Millet, *Appl. Catal. A* **2005**, *279*, 67–77.